

Geophysical Research Letters

RESEARCH LETTER

10.1029/2019GL085014

Key Points:

- The electron nongyrotropic distribution depended on the energy and the normal distance from the midplane of the electron diffusion region
- The electron crescent distributions were caused by the meandering motion and the Hall electric field together
- The fine substructures were observed in the narrow electron diffusion region

Correspondence to:

R. Wang and Q. Lu,
rswan@ustc.edu.cn;
qmlu@ustc.edu.cn

Citation:

Li, X., Wang, R., Lu, Q., Hwang, K.-J., Zong, Q., Russell, C. T., & Wang, S. (2019). Observation of nongyrotropic electron distribution across the electron diffusion region in the magnetotail reconnection. *Geophysical Research Letters*, *46*, 14,263–14,273. <https://doi.org/10.1029/2019GL085014>

Received 15 AUG 2019

Accepted 17 DEC 2019

Accepted article online 19 DEC 2019

Published online 26 DEC 2019

Observation of Nongyrotropic Electron Distribution Across the Electron Diffusion Region in the Magnetotail Reconnection

Xinmin Li^{1,2} , Rongsheng Wang^{1,2} , Quanming Lu^{1,2}, Kyoung-Joo Hwang³ , Qiugang Zong⁴, Christopher T. Russell⁵, and Shui Wang^{1,2}

¹CAS Key Laboratory of Geospace Environment, Department of Geophysics and Planetary Science, University of Science and Technology of China, Hefei, China, ²CAS Center for Excellence in Comparative Planetology, Hefei, China, ³Southwest Research Institute, San Antonio, TX, USA, ⁴Institute of Space Physics and Applied Technology, Peking University, Beijing, China, ⁵Earth Planetary and Space Sciences, University of California, Los Angeles, CA, USA

Abstract Using measurements by the Magnetospheric Multiscale spacecraft in the magnetotail, we studied electron distribution functions across an electron diffusion region. The dependence of the nongyrotropic distribution on the energy and vertical distance from the electron diffusion region midplane was revealed for the first time. The nongyrotropic distribution was observed everywhere except for an extremely narrow layer right at the electron diffusion region midplane. The energy of the nongyrotropic distribution increased with growth of the vertical distance from the midplane. For the electrons within certain energy range, they exhibited the nongyrotropic distribution at the distance further away from the midplane than that expected from the meandering motion. The correlation between the crescent-shaped distribution with multiple stripes and the large Hall electric field was established. It appears that the measured nongyrotropic distribution and the crescent-shaped distribution were caused by the meandering motion and the Hall electric field together.

Plain Language Summary The Magnetospheric Multiscale mission is designed to study electron physics of magnetic reconnection, a key process for many explosive phenomena in solar flares and magnetosphere. Understanding electron motion is highly important in the study of magnetic reconnection, and the electron velocity distribution is an intuitive and effective way to study the electron dynamics. In this paper, we present a complete electron diffusion region crossing by Magnetospheric Multiscale during a nearly symmetric magnetic reconnection in the magnetotail and show the evolution of the electron velocity distributions across the electron diffusion region. In addition, the relationship between Hall electric field and crescent-shaped electron distribution is also shown in this paper.

1. Introduction

Magnetic reconnection is a fundamental plasma process, by which magnetic energy can be effectively converted into plasma kinetic and thermal energy in space and astrophysical and laboratory plasmas (Yamada et al., 2010). In collisionless environments, magnetic reconnection includes multiscale process in the current sheet. A particular interesting area is the electron diffusion region (EDR), surrounding the X-line, where the electron frozen-in condition was broken, resulting in the reconfiguration of the magnetic field topology. Numerous simulations predicted that the EDR corresponded to the electron current layer formed by the electron flows along the X-line (e.g., Fu et al., 2006; Pritchett, 2001; Hesse et al., 2014; Torbert et al., 2016). Direct measurements of the EDR were few before the launch of the Magnetospheric Multiscale (MMS) mission (Burch, Moore, et al., 2016).

Based on accurate measurements of electron velocity distribution function (VDF) from MMS, Burch, Torbert, et al. (2016) first reported the crescent-shaped electron distribution in the plane perpendicular to the magnetic field in close proximity to an EDR at the magnetopause, which was predicted as one distinct EDR feature in asymmetric reconnection simulations (Bessho et al., 2016; Bessho et al., 2017; Cassak et al., 2017; Hesse et al., 2014; Hesse et al., 2016; Lapenta et al., 2017; Shay et al., 2016). The following study of tens of EDR events at the magnetopause further confirmed this kind of electron

distribution (Chen et al., 2017; Egedal et al., 2016; Genestreti et al., 2017; Hwang et al., 2017; Phan et al., 2016; Webster et al., 2018). A few mechanisms were proposed to interpret such distribution, such as meandering (cusp-like) electron orbits (Hesse et al., 2014; Lapenta et al., 2017; Shay et al., 2016) and a drift-kinetic model (Egedal et al., 2016). Most recently, the crescent-shaped electron distribution was detected in the EDR of a symmetric reconnection in the magnetotail as well (Torbert et al., 2018; Zhou et al., 2019), as predicted by numerical simulations (e.g., Bessho et al., 2018). Moreover, multiple discrete striation of the crescent-shaped and the triangle-shaped in the electron distribution functions were measured and attributed to multiple meandering bounces in the diffusion region (Bessho et al., 2018; Torbert et al., 2018).

In this letter, we present a complete EDR crossing in the magnetotail, which was reported recently by Zhou et al. (2019). Thus, the evolution of electron VDFs across the EDR can be investigated in detail, which was crucial to finally reveal mechanisms of the special distribution at the EDR. The nongyrotropic electron distribution was always observed inside the EDR except for an extremely narrow layer at the EDR midplane. The dependence of such a distribution on the electron energy and the normal distance from the EDR midplane was quantified. The direct relation between the crescent-shaped VDFs and the large Hall electric field was established.

2. Instruments and Database

The data from several instruments onboard MMS are used in this letter. The magnetic field data are from the Flux Gate Magnetometer with a time resolution of 128 Hz (Russell et al., 2016). The plasma data are taken from the Fast Plasma investigation with a 150 ms time resolution for ions and 30 ms for electrons (Pollock et al., 2016). The electric field data with a time resolution of 8,192 Hz are obtained from the electric field double probe (Ergun et al., 2016; Lindqvist et al., 2016). The separation of the four satellites was only ~ 20 km during the interesting event, and the measurements at all four satellites were almost the same, thus only the data at MMS 2 were used in this letter.

3. Observation and Analysis

At $\sim 12:18:32$ UT on 10 August 2017, the spacecraft MMS was located at $[-15.2, 2.64, 4.8]R_e$ in the Geocentric Solar Ecliptic coordinate system and crossed the magnetotail plasma sheet twice during 12:18:00–12:19:00 UT (Figures 1a and 1g). In this interval, MMS traversed the plasma sheet from the Southern Hemisphere to the Northern Hemisphere and then returned to the Southern Hemisphere again (Figure 1a). We mainly focused on the first crossing at $\sim 12:18:33$ UT. The local current coordinate system was obtained from the hybrid method. The normal direction N was obtained from the maximum direction derivative of magnetic field (MDD-B) (Shi et al., 2005), M was defined as $M = N \times L_{MVA}$ where the L_{MVA} was the maximum direction of the minimum variance analysis of magnetic field (MVA-B) (Sonnerup & Scheible, 1998) and the L completed the right-handed system. As a result, the local current coordinate was $L = [0.9617, -0.1762, -0.2099]$, $M = [0.2522, 0.8686, 0.4266]$, and $N = [0.1071, -0.4632, 0.8798]$ relative to Geocentric Solar Ecliptic coordinate, different from that in Zhou et al. (2019).

Figure 1b shows the ion flows in the rest frame of the current sheet during the first crossing, and the velocity of the current sheet was obtained from the timing method (Schwartz, 1998), $V_N = [-0.4, -1.6, -38.4]$ km/s. The spacecraft initially observed the tailward ion flow (blue trace, $v_{iL} > -300$ km/s) and then the earthward flow ($v_{iL} < 200$ km/s). The v_{iL} reversal point was just detected at the center of the current sheet ($B_L \sim 0$ nT), that is, the vertical dashed line. In the meantime, the ion flows in the M direction was persistently positive in the whole crossing ($v_{iM} \sim 300$ km/s, green trace), while the electron flows v_{eM} were negative and substantially enhanced (Figure 1c), down to $-10,000$ km/s $\approx -0.25 V_{Ae}$ at the reversal point of v_{iL} and B_L , where V_{Ae} equaled to $\sim 42,400$ km/s, based on $N = 0.14$ cm $^{-3}$ and $|B| = 17$ nT. The electric field E_N was positive in the Southern Hemisphere and became negative in the Northern Hemisphere (Figure 1d), in agreement with the Hall electric field. The observation indicates that a retreating reconnection event was encountered by the spacecraft.

The ion flows v_{iN} were basically positive in the Southern Hemisphere and negative in the Northern Hemisphere (red curve, Figure 1b), meaning that the ion inflows were observed in this crossing and the

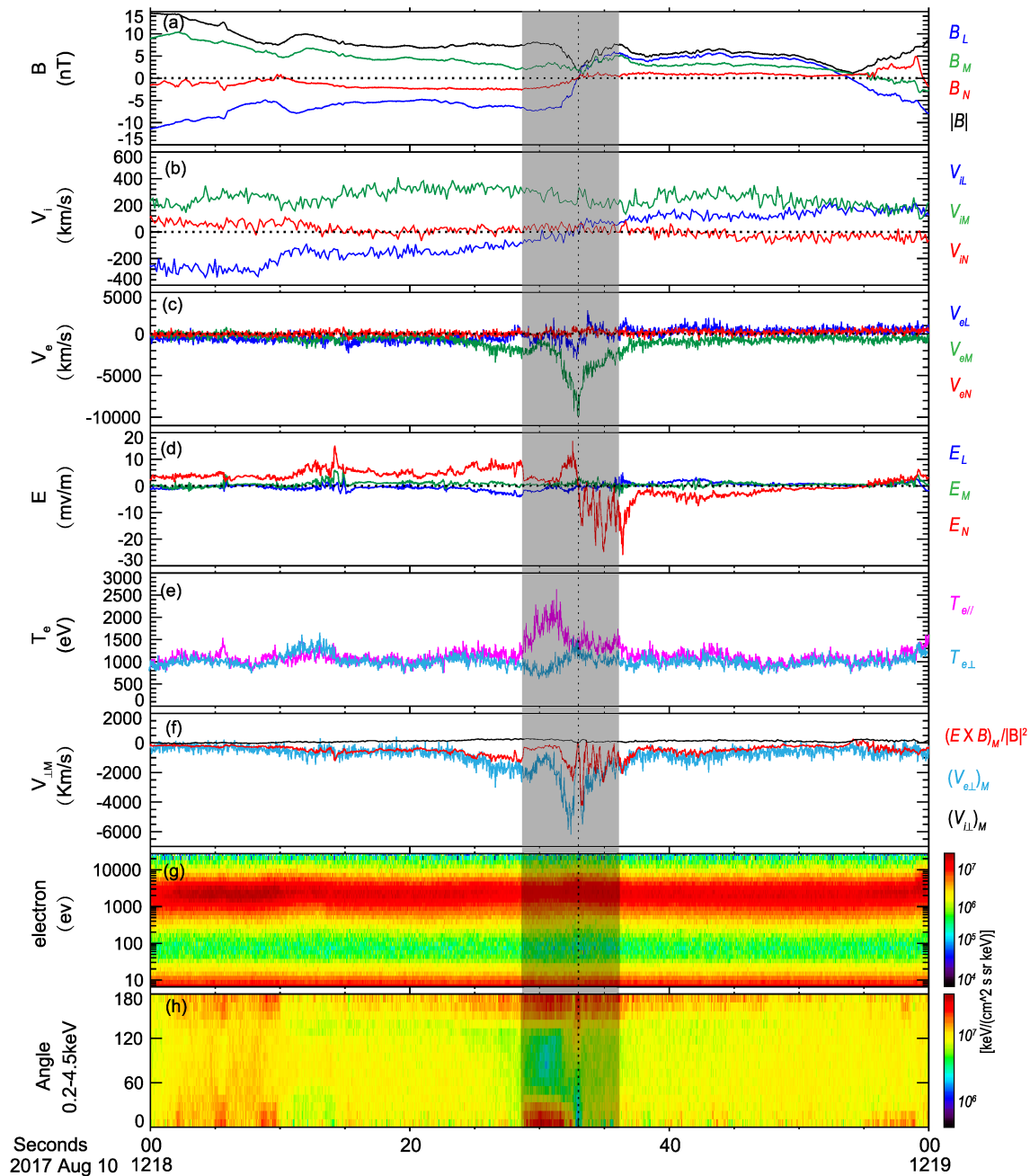


Figure 1. (a) Three components and magnitude of the magnetic field, (b) the ion bulk flows in the rest velocity frame of the current sheet, (c) the electron bulk flows, (d) three components of electron field, (e) parallel and perpendicular electron temperature, (f) V_{eL} , V_{iL} , and V_{EXB} in M direction, (g) electron omnidirectional differential energy flux, and (h) electron pitch angle distribution during 0.2–4.5 KeV.

maximum inflowing speed was up to ~ 120 km/s. At the reversal point of B_L , V_{iL} , and E_N , the intense electron flows V_{eM} should be the EDR of this reconnection. In order to confirm this point, the electron demagnetization condition ($E + V_e \times B \neq 0$) was checked. For simplicity, only the M component was shown in Figure 1f. It is clear that the measured electron velocity was significantly different from the electric field drift velocity between 12:18:28.7 and 12:18:36.0 UT (the shadow area). Thus, it is concluded that the spacecraft crossed the EDR from the south to the north. B_M (green trace in Figure 1a) was always positive and dipped to ~ 2 nT at the EDR center. It means a ambient guide field of $B_g \sim 2$ nT in this reconnection, and the ratio of B_g/B_0 was ~ 0.1 , where B_0 was the reconnecting magnetic field (~ 17 nT).

Inside the EDR, the electron temperature T_e (Figure 1e) showed strongly anisotropic, especially in its southern part (12:18:28.7–12:18:32.9 UT) where $T_{e\parallel}$ (up to 2.3 keV) was much larger than $T_{e\perp}$ (less than 1.5 keV). In the northern part (12:18:33.05–12:18:36.0 UT), the anisotropic temperature was still clear, whereas $T_{e\parallel}$ was only slightly higher than $T_{e\perp}$. At the center of the EDR (12:18:32.9–12:18:33.05 UT) where $B_L \approx 0$, $T_{e\perp}$ was raised and nearly equal to $T_{e\parallel}$. Figure 1h shows the electron pitch angle distribution at the energy range from 0.2 to 4.5 keV. The electron pitch angle distribution showed the distinct feature between subregions of the EDR. The electron differential energy fluxes were significantly enhanced in the field-aligned directions ($\sim 0^\circ$ and $\sim 180^\circ$) and depressed around the perpendicular direction ($\sim 90^\circ$) in the southern part, leading to the field-aligned bidirectional distribution. At its center part, the fluxes were enhanced only at $\sim 180^\circ$ direction, and thus, an electron beam was observed. In the northern part, the flux enhancement was observed only along the 180° direction, dramatically different from the distribution in the southern part. Another distinction between the southern and northern parts was the electric field fluctuations. The large-amplitude fluctuations ($\delta E \sim 20$ mV/m) were measured only in the Northern Part B_N (Figure 1d). Given the distinct features across the EDR, the EDR was divided into three parts (12:18:28.7–12:18:32.9 UT as B_S, 12:18:32.9–12:18:33.05 UT as C, and 12:18:33.05–12:18:36.0 UT as B_N), illustrated in Figure 2a and labeled as the gray and red bars at the top of Figure 2b.

The parallel and perpendicular electron velocities gradually increased as the spacecraft approached the EDR center in the Part B_S and gradually decayed as MMS moved away from the center in the Part B_N (Figure 2c). At the Center Part C, the parallel velocity got its maximum values, while the perpendicular velocity sharply dipped there. The deviation between the measured electron velocity in the perpendicular direction $\mathbf{V}_{e\perp}$ and the electric field drift velocity $\mathbf{V}_E \times \mathbf{B}$ was quite obvious in the southern and northern parts of the EDR (Figures 2d–2f). In contrast, they matched pretty well in the Part C. The energy conversion $\mathbf{J} \cdot (\mathbf{E} + \mathbf{V}_e \times \mathbf{B})$ and its parallel ($j_{\parallel} \cdot E_{\parallel}$) as well as perpendicular ($\mathbf{J}_{\perp} \cdot (\mathbf{E} + \mathbf{V}_e \times \mathbf{B})_{\perp}$) components were displayed in Figure 2g. The energy conversion of $\mathbf{J} \cdot (\mathbf{E} + \mathbf{V}_e \times \mathbf{B})$ was significant inside the EDR and predominated in the Parts of C and B_N. Namely, the energy conversion was weak in the Part B_S and became substantial in the Parts of C and B_N. The perpendicular component $\mathbf{J}_{\perp} \cdot (\mathbf{E} + \mathbf{V}_e \times \mathbf{B})_{\perp}$ was strong in the Part B_N (up to 0.7 nW/m³) and negligible in the Parts C and B_S. The parallel component peaked inside the Part C (~ 0.5 nW/m³) and was basically negative in the Part B_N. The parallel electric field and its error were shown in Figure 2h. E_{\parallel} had a peak (~ 3.2 mV/m) larger than its error in the Part C where $B_L \approx 0$ and $B_{\text{tot}} \approx B_M$. Therefore, the parallel electric field could be regarded as reconnection electric field E_M . The maximum rate was calculated by $\frac{E_M}{v_{iA} B_0} \approx 0.19$, consistent with the estimation of $v_{in}/v_{iA} \sim 0.15$.

The electron VDFs in the perpendicular plane were examined inside the EDR. Because the electrons with different energies displayed the distinguishable feature, the energy range was divided into three segments: the high energy (3×10^4 – 4×10^4 km/s, $\sim 2,560$ – $4,550$ eV), the medium energy (2×10^4 – 3×10^4 km/s, $\sim 1,140$ – $2,560$ eV), and the low energy (0.2×10^4 – 2×10^4 km/s, ~ 70 – $1,140$ eV), marked with dashed concentric circles on each plot. The VDFs displayed apparent difference in the three parts. In the Southern Part B_S, B_L was approximately -7.0 nT at $\sim 12:18:29$ UT, got the minimum value of approximately -8.0 nT at $\sim 12:18:30$ UT, and then gradually increased from -8 to 0 nT (Figure 3a). It means that the spacecraft was near the EDR edge at $\sim 12:18:30$ UT and got the center at $\sim 12:18:33$ UT. So the half-thickness of the EDR was estimated to be $(38.4 \text{ km/s} \times 3 \text{ s}) \approx 8d_e$. Prior to $\sim 12:18:30$ UT, the spacecraft was close to the edge of the EDR. The nongyrotropic electron distribution was observed in the whole interval of the Part B_S. At the EDR edge, the high-energy electrons displayed a clear nongyrotropic distribution, while the medium- and low-energy electrons exhibited nearly gyrotropic distribution (Figure 3d1). Afterward, the medium-energy electrons began to be the nongyrotropic distribution as well at $\sim 12:18:31$ UT (Figure 3d2), and the low-energy electrons were still gyrotropic. During 12:18:30.658–12:18:31.858 UT as the spacecraft approached the EDR center, the nongyrotropic distribution for the high- and medium-energy electrons became clearer and clearer and the gyrotropic distribution for the low-energy electrons were still observed (Figures 3d2 and 3d3). The low-energy electrons began to show the nongyrotropic distribution from $\sim 12:18:32.128$ UT (Figure 3d4) and became evident at $\sim 12:18:32.638$ UT (Figure 3d5). It seems that the electron distribution depended on the energy and the normal distance from the midplane of the EDR ($B_L = 0$ nT). Inside the Part C, the electrons in all energy range displayed nearly gyrotropic distribution (Figure 3d6), totally different from that in the Part B_S.

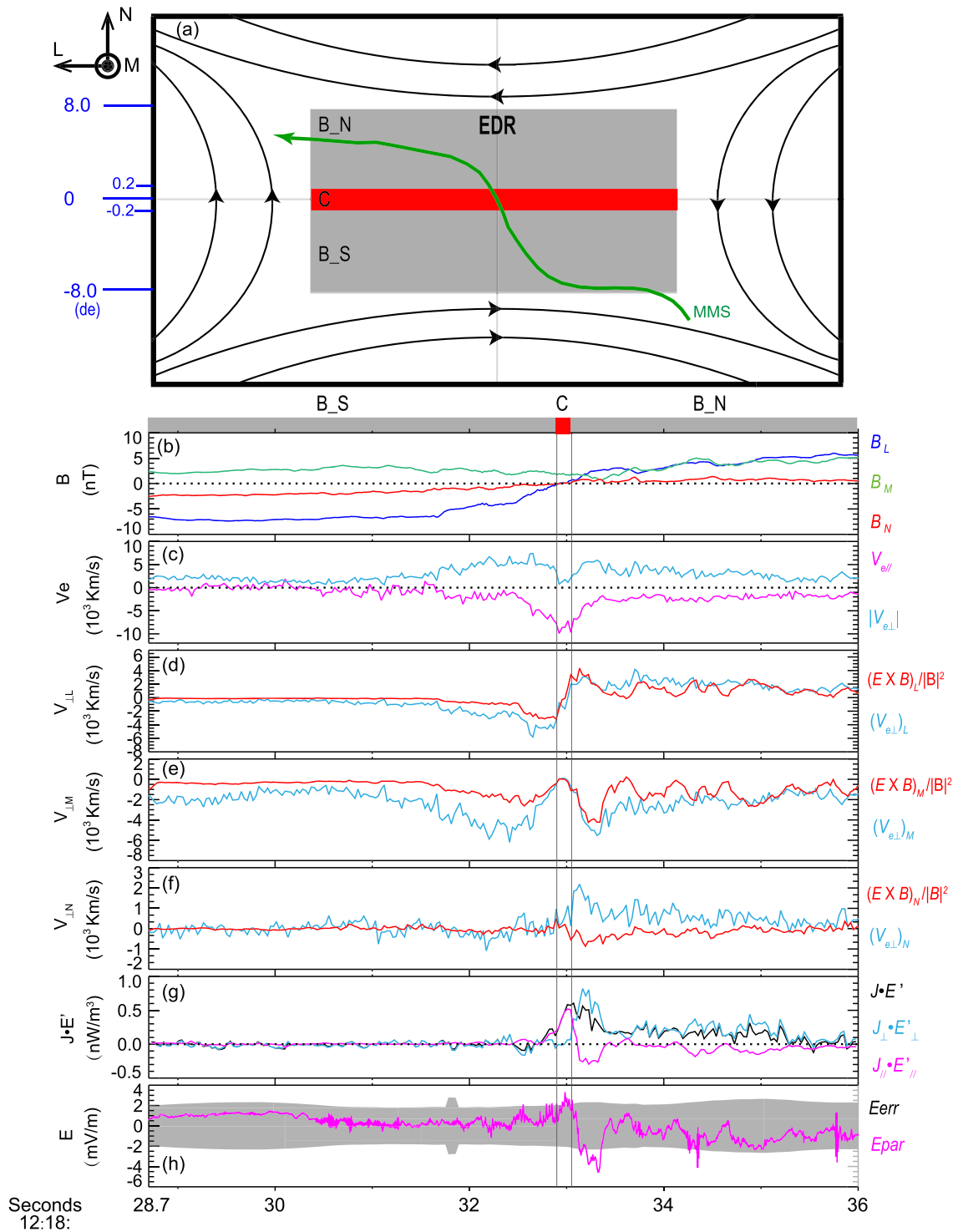


Figure 2. (a) A schematic illustration for the EDR partition and the crossing path of MMS2, (b) three components of the magnetic field, (c) electron bulk flows in parallel and perpendicular direction, (d–f) three components of $V_{e\perp}$, $V_{i\perp}$, and $V_{E \times B}$, (g) the total energy conversion and its parallel as well as perpendicular components, and (h) parallel electric field with its error.

In order to quantitate the dependence, we defined a term called pseudo-agyrotropy: the ratio of the integrated electron fluxes between the right sector ($V_{\perp 2} > 0$) and the left sector ($V_{\perp 2} < 0$) for the three energy ranges (shown in Figure 3c). The value of the pseudo-agyrotropy for the high-energy electrons

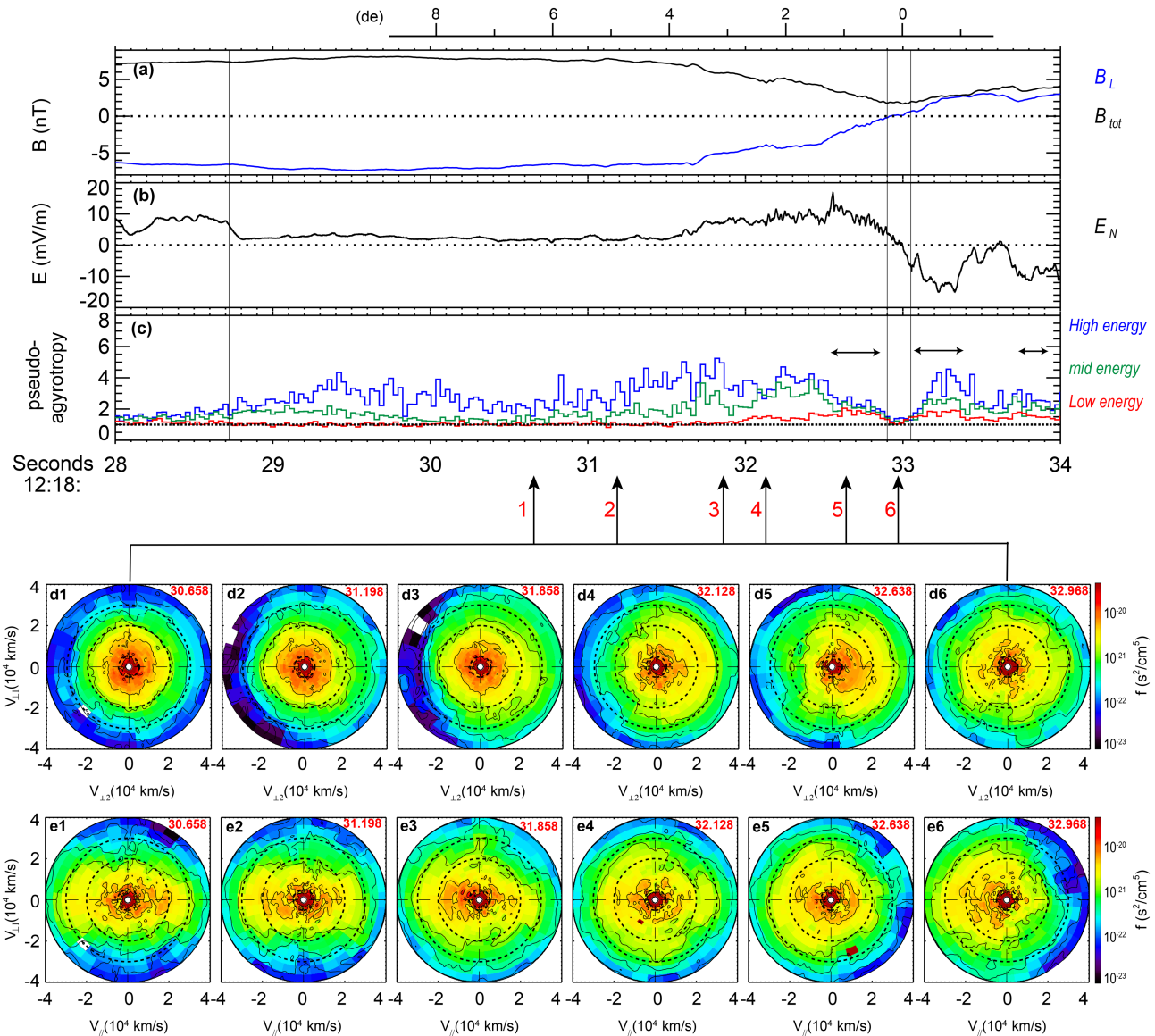


Figure 3. (a) B_L and B_{tot} ; (b) E_N ; (c) the pseudo-agyrotropy of different energy segments in perpendicular plane: high energy (3×10^4 – 4×10^4 km/s), medium energy (2×10^4 – 3×10^4 km/s), and low energy (0.5×10^4 – 2×10^4 km/s); (d) VDFs in perpendicular plan, $V_{\perp 1} = (b \times v)$ and $V_{\perp 2} = (b \times v) \times b$; and (e) VDFs in parallel plan, $V_{\perp 1} = (b \times v)$ and $V_{\parallel} = b$, where b and v are unit vectors of B and V_e . The radius of black dashed circle are 0.5×10^4 , 2×10^4 , and 3×10^4 km/s, respectively. The scale indicating the normal distance from the midplane of EDR is marked at the top of the Figure 3, and the horizontal arrows mark the time of the crescent VDFs.

was ~ 2 at the EDR edge ($\sim 12:18:30$ UT), gradually increased and peaked at $\sim 12:18:31.828$ UT, and then decreased as the spacecraft approached the EDR midplane. The pseudo-agyrotropy of the medium- and low-energy electrons exhibited a similar evolution in this process (green and red traces). However, they began to become significant (>1.5) and peaked at different times from that of the high-energy electrons. The pseudo-agyrotropy of the medium- and low-energy electrons became to be larger than 1.5 at 12:18:30.8 UT ($\sim 6.0 d_e$ away from the midplane) and 12:18:32.0 UT ($\sim 2.7 d_e$ away from the midplane), respectively. The pseudo-agyrotropy of the high-, medium-, and low-energy electrons peaked at $\sim 3.2 d_e$, $\sim 1.5 d_e$, and $\sim 0.9 d_e$ away from the midlane of the EDR, respectively. In the Center Part C, all of the pseudo-agyrotropy decreased to be ~ 1 . The observations indicate that the nongyrotropic distribution extended from high- to low-energy electrons as the spacecraft approached the EDR midplane.

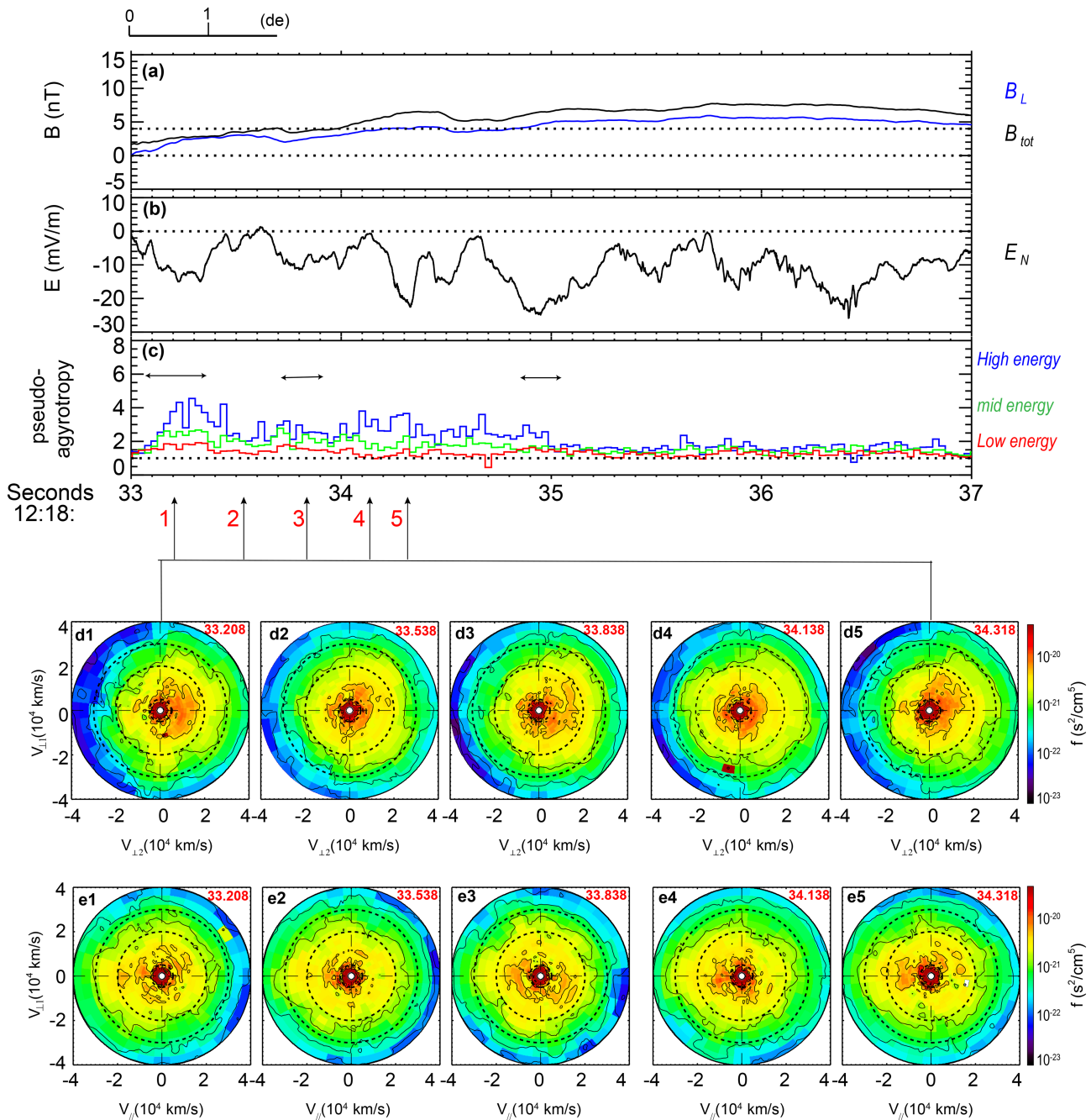


Figure 4. The figure format is the same as Figure 3.

The crescent-shaped electron distribution was observed in the perpendicular plane during 12:18:32.5–12:18:32.9 UT of the Part B_S, consistent with the interval with the largest values of pseudo-agyrotropy for the low-energy electrons, and disappeared at the right center of the EDR. In most cases, the multiple crescent-shaped distribution was observed, as shown in Figure 3d5.

The electron distribution in the $v_{\parallel} - v_{\perp 1}$ plane was shown in Figure 3e. It displayed the field-aligned bidirectional distribution at the edge of the EDR (Figures 3e1 and 3e2). As the spacecraft approached the EDR midplane, the fluxes in the antiparallel direction became stronger and stronger (Figures 3e3–3e5). At last, it became the beam distribution in the Part C or the so-called triangle distribution (Bessho et al., 2018; Torbert et al., 2018).

The similar dependence of the electron distribution on the distance from the EDR midplane was found in the Part B_N but modified by the large-amplitude fluctuations of electric field, as shown in Figure 4. The pseudo-agyrotropy for the electrons with all three energy ranges were significant during the first two seconds 12:18:33–12:18:35 UT (Figure 4c) with several repeated enhancements of $|E_N|$ (the so-called E_N valleys later; Figure 4b), consistent with the nongyrotropic distribution (Figures 4d1–4d5). Furthermore, the close correlation between the enhancements of the pseudo-agyrotropy for the low-energy electrons (red trace in Figure 4c) and the large absolute values of E_N (Figure 4b) was found. It suggested that the low-energy electron nongyrotropic distribution was strongly affected by the E_N .

After examining the electron distribution functions, we found that the crescent-shaped distribution lasted for a while (>200 ms), while E_N kept inside the valleys ($|E_N| \geq 10$ mV/m), for example, during 12:18:33.1–12:18:33.4 UT, 12:18:33.7–12:18:33.9 UT, and 12:18:34.9–12:18:35.1 UT marked by the horizontal arrows in Figure 4c, and disappeared, while E_N was close to zero (Figures 4d2 and 4d4). During the other two short valleys of E_N around 12:18:34.4 UT, the crescent-shaped distribution was observed as well (Figure 4d5) but only lasted for one and two collecting times. After 12:18:35 UT when MMS was $5 d_e$ away from the EDR midplane, the crescent-shaped distribution was no longer observed again, although multiple E_N valleys were observed repeatedly. It seems that the crescent-shaped distribution was largely affected by the intense E_N . The field-aligned bidirectional distribution which was very clear in the Part B_S disappeared in the Part B_N, and the triangle distribution in the left sector ($v_{L2} < 0$) was clear (Figures 4e1–4e5). It seems that the electrons in the parallel direction were scattered, resulting in disappearance of the bidirectional distribution.

4. Discussion and Summary

A few EDR events during symmetric reconnection have been reported recently, based on the MMS observations in the magnetotail (Chen et al., 2019; Genestreti et al., 2018; Nakamura et al., 2018; Torbert et al., 2018; Wang et al., 2018; Zhou et al., 2019). However, a direct crossing of the EDR was rare (Wang et al., 2018; Zhou et al., 2019). In this letter, we present a complete crossing of the EDR in the magnetotail, with a moderate guide field of ~ 0.1 . The EDR was tightly structured and divided into three parts according to the distinct features. In the southern part, the electrons were mainly heated in the field-aligned direction, the parallel temperature was substantially larger than the perpendicular component, and the field-aligned bidirection distribution was detected. In the northern part, the electrons were heated in both field-aligned and perpendicular directions, the parallel temperature was slightly larger than the perpendicular temperature, and the beam-like distribution primarily antiparallel to magnetic field was observed. Moreover, the large-amplitude electrostatic fluctuation was observed only in the northern part, which could be the reason for the different electron behavior in the two parts. And the crossing of the southern/tailward separatrix (not shown) was also a possible reason for the difference (Bourdin, 2017). The thickness of this EDR was up to $\sim 16.0 d_e$, much thicker than $\sim 1.0 d_e$ of previous observations (e.g., Torbert et al., 2018) and simulation results (e.g., Hesse et al., 1999). Given the reconnection rate and the thickness of the EDR, the EDR elongation in the outflow direction was estimated to be $\sim 80 d_e$.

Between the southern and northern parts, there was an extremely narrow layer (high-width was $\sim 0.2 d_e$), namely, the Center Part C. In both southern and northern parts, the deviation between $\mathbf{V}_{e\perp}$ and $\mathbf{E} \times \mathbf{B}$ was substantial in one or all directions. However, the two terms matched very well in the Narrow Center Part C. Furthermore, the parallel electron speed got the maximum value, and the perpendicular speed was close to 0 in the Part C. The energy conversion primarily originated from the parallel component in the Part C, was dominated by the perpendicular component in the Part B_N, and was negligible in the Part B_S. The strong energy conversion in the perpendicular direction in the Part B_N directly related to the large amplitude electrostatic fluctuations therein.

The nongyrotropic electron distribution was common inside the EDR. It could be observed $\sim 8.0 d_e$ away from the EDR midplane for the high-energy electrons, appeared at $\sim 5.9 d_e$ away from the EDR midplane for the medium-energy electrons, and confined to be within $\sim 3.0 d_e$ away from the midplane for the low-energy electrons. In the right center part of the EDR, the electrons displayed the

gyrotropic distribution. Therefore, it appears that the nongyrotropic distribution was caused by the electron meandering motion. The electrons with the higher energy had the larger gyroradius and thus were observed further away from the EDR midplane. According to the observations in the EDR, the profile of $B_L(N)$ was used to calculate the trajectory of the meandering motion. Then, the maximum gyroradius corresponding to the high-, medium-, and low-energy meandering electrons were of $4.5 d_e$, $3.6 d_e$, and $2.9 d_e$, respectively. However, the fact is that the nongyrotropic electrons were observed further away from the expected location of the meandering motion, relative to the EDR midplane. In other words, the meandering motion alone cannot explain the observed nongyrotropic electron distribution inside the EDR. The Hall electric field must play an important role for the observed nongyrotropic electron distribution as well. Furthermore, the electrons experiencing the meandering motion would bounce between two hemispheres of the EDR and thus display the gyrotropic distribution in the central region between two hemispheres, which explains the gyrotropic distribution in the Center Part C. The electron curvature scattering was another possible explanation for the gyrotropic distribution at the EDR center (Zhou et al., 2019).

The crescent-shaped electron distribution was indeed observed inside the EDR but only in the region with large electric field E_N , which was clearly discerned in the northern part with large amplitude electrostatic fluctuations in the N direction. In most cases, the crescent-shaped distribution was multiple stripes. Bessho et al. (2018) suggested that the multiple stripes were due to multiple meandering bounces caused by the reconnection electric field, and the separation between stripes became larger as the Hall electric field increased in the symmetric reconnection. So the multiple stripes were easily distinguished in the region with the large electric field E_N , consistent with our observations. For asymmetric reconnection, the connection between the energy of the crescent distribution and the acceleration by the monopole Hall electric field had been confirmed by the recent observation (Pritchard et al., 2019).

There was an ambient guide field in our EDR event. Hence, the reconnection electric field became to be a parallel electric field near the EDR center, exceeded 3.0 mV/m, and thus, the reconnection rate was calculated to be as large as 0.19 , consistent with the previous estimation (Genestreti et al., 2018; Liu et al., 2017; Nakamura et al., 2018; Xiao et al., 2006). The relation among reconnection rate, electron dynamics, and guide field had been established in previous study (Chen et al., 2019). The electron acceleration by the reconnection electric field was very evident inside the EDR, and the acceleration was most pronounced at the EDR center with an intense generated electron beam along the X-line. The speed of the beam was up to $-0.25 V_{Ae}$. We checked the higher-energy electron data in the EDR as well and did not find any obvious acceleration evidence.

In conclusion, we studied a complete crossing of an EDR event in the magnetotail with a moderate guide field. The EDR was tightly structured although its half-thickness was only about $8.0 d_e$. Along the magnetic field direction, the electrons were bidirectional in the southern part, showed the beam-like distribution in the northern part, and exhibited the beam distribution antiparallel to magnetic field in the center part. In the perpendicular plane, the nongyrotropic distribution was observed in both the southern and the northern parts and vanished in the center part. The nongyrotropic distribution depended on the electron energy and the normal distance from the EDR midplane and was caused by the meandering motion and the Hall electric field. The multiple crescent-shaped electron distribution directly related to the large Hall electric field.

Acknowledgments

All the MMS data used in this work are available at the MMS data center (<https://lasp.colorado.edu/mms/sdc/>). This work is supported by the National Science Foundation of China (NSFC) grants (41674143, 41474126, 41331067, and 41421063) and by the National Basic Research Program of China (2013CBA01503).

References

- Bessho, N., Chen, L. J., & Hesse, M. (2016). Electron distribution functions in the diffusion region of asymmetric magnetic reconnection. *Geophysical Research Letters*, *43*, 1828–1836. <https://doi.org/10.1002/2016GL067886>
- Bessho, N., Chen, L. J., Hesse, M., & Wang, S. (2017). The effect of reconnection electric field on crescent and U-shaped distribution functions in asymmetric reconnection with no guide field. *Physics of Plasmas*, *24*(7), 072903. <https://doi.org/10.1063/1.4989737>
- Bessho, N., Chen, L. J., Wang, S., & Hesse, M. (2018). Effect of the reconnection electric field on electron distribution functions in the diffusion region of magnetotail reconnection. *Geophysical Research Letters*, *45*, 12142–12152. <https://doi.org/10.1029/2018GL081216>
- Bourdin, P. A. (2017). Catalog of fine-structured electron velocity distribution functions. Part 1: Antiparallel magnetic-field reconnection (Geospace Environmental Modeling case). *Annales Geophysicae*, *35*(5), 1051–1067. <https://doi.org/10.5194/angeo-35-1051-2017>
- Burch, J. L., Moore, T. E., Torbert, R. B., & Giles, B. L. (2016). Magnetospheric Multiscale overview and science objectives. *Space Science Reviews*, *199*(1–4), 5–21. <https://doi.org/10.1007/s11214-015-0164-9>
- Burch, J. L., Torbert, R. B., Phan, T. D., Chen, L. J., Moore, T. E., Ergun, R. E., et al. (2016). Electron-scale measurements of magnetic reconnection in space. *Science*, *352*(6290), aaf2939. <https://doi.org/10.1126/science.aaf2939>

- Cassak, P. A., Genestreti, K. J., Burch, J. L., Phan, T. D., Shay, M. A., Swisdak, M., et al. (2017). The effect of a guide field on local energy conversion during asymmetric magnetic reconnection: Particle-in-cell simulations. *Journal of Geophysical Research: Space Physics*, *122*, 11,523–11,542. <https://doi.org/10.1002/2017JA024555>
- Chen, L. J., Hesse, M., Wang, S., Gershman, D., Ergun, R. E., Burch, J., et al. (2017). Electron diffusion region during magnetopause reconnection with an intermediate guide field: Magnetospheric Multiscale observations. *Journal of Geophysical Research: Space Physics*, *122*, 5235–5246. <https://doi.org/10.1002/2017JA024004>
- Chen, L. J., Wang, S., Hesse, M., Ergun, R., Moore, T., Giles, B., et al. (2019). Electron diffusion regions in magnetotail reconnection under varying guide fields. *Geophysical Research Letters*, *46*, 6230–6238. <https://doi.org/10.1029/2019GL082393>
- Egedal, J., Le, A., Daughton, W., Wetherton, B., Cassak, P. A., Chen, L. J., et al. (2016). Spacecraft observations and analytic theory of crescent-shaped electron distributions in asymmetric magnetic reconnection. *Physical Review Letters*, *117*(18), 185101. <https://doi.org/10.1103/PhysRevLett.117.185101>
- Ergun, R. E., Holmes, J. C., Goodrich, K. A., Wilder, F. D., Stawarz, J. E., Eriksson, S., et al. (2016). Magnetospheric Multiscale observations of large-amplitude, parallel, electrostatic waves associated with magnetic reconnection at the magnetopause. *Geophysical Research Letters*, *43*, 5626–5634. <https://doi.org/10.1002/2016GL068992>
- Fu, X. R., Lu, Q. M., & Wang, S. (2006). The process of electron acceleration during collisionless magnetic reconnection. *Physics of Plasmas*, *13*(1), 012309. <https://doi.org/10.1063/1.2164808>
- Genestreti, K. J., Burch, J. L., Cassak, P. A., Torbert, R. B., Ergun, R. E., Varsani, A., et al. (2017). The effect of a guide field on local energy conversion during asymmetric magnetic reconnection: MMS observations. *Journal of Geophysical Research: Space Physics*, *122*, 11,342–11,353. <https://doi.org/10.1002/2017JA024247>
- Genestreti, K. J., Nakamura, T. K. M., Nakamura, R., Denton, R. E., Torbert, R. B., Burch, J. L., et al. (2018). How accurately can we measure the reconnection rate E-M for the MMS diffusion region event of 11 July 2017? *Journal of Geophysical Research: Space Physics*, *123*, 9130–9149. <https://doi.org/10.1029/2018JA025711>
- Hesse, M., Aunai, N., Birn, J., Cassak, P., Denton, R. E., Drake, J. F., et al. (2016). Theory and modeling for the Magnetospheric Multiscale Mission. *Space Science Reviews*, *199*(1–4), 577–630. <https://doi.org/10.1007/s11214-014-0078-y>
- Hesse, M., Aunai, N., Sibeck, D., & Birn, J. (2014). On the electron diffusion region in planar, asymmetric, systems. *Geophysical Research Letters*, *41*, 8673–8680. <https://doi.org/10.1002/2014GL061586>
- Hesse, M., Schindler, K., Birn, J., & Kuznetsova, M. (1999). The diffusion region in collisionless magnetic reconnection. *Physics of Plasmas*, *6*(5), 1781–1795. <https://doi.org/10.1063/1.873436>
- Hwang, K. J., Sibeck, D. G., Choi, E., Chen, L. J., Ergun, R. E., Khotyaintsev, Y., et al. (2017). Magnetospheric Multiscale mission observations of the outer electron diffusion region. *Geophysical Research Letters*, *44*, 2049–2059. <https://doi.org/10.1002/2017GL072830>
- Lapenta, G., Berchem, J., Zhou, M., Walker, R. J., el-Alaoui, M., Goldstein, M. L., et al. (2017). On the origin of the crescent-shaped distributions observed by MMS at the magnetopause. *Journal of Geophysical Research: Space Physics*, *122*, 2024–2039. <https://doi.org/10.1002/2016JA023290>
- Lindqvist, P. A., Olsson, G., Torbert, R. B., King, B., Granoff, M., Rau, D., et al. (2016). The spin-plane double probe electric field instrument for MMS. *Space Science Reviews*, *199*(1–4), 137–165. <https://doi.org/10.1007/s11214-014-0116-9>
- Liu, Y.-H., Hesse, M., Guo, F., Daughton, W., Li, H., Cassak, P. A., & Shay, M. A. (2017). Why does steady-state magnetic reconnection have a maximum local rate of order 0.1? *Physical Review Letters*, *118*, 085101. <https://doi.org/10.1103/PhysRevLett.118.085101>
- Nakamura, T. K. M., Genestreti, K. J., Liu, Y. H., Nakamura, R., Teh, W. L., Hasegawa, H., et al. (2018). Measurement of the magnetic reconnection rate in the Earth's magnetotail. *Journal of Geophysical Research: Space Physics*, *123*, 9150–9168. <https://doi.org/10.1029/2018JA025713>
- Phan, T. D., Eastwood, J. P., Cassak, P. A., Øieroset, M., Gosling, J. T., Gershman, D. J., et al. (2016). MMS observations of electron-scale filamentary currents in the reconnection exhaust and near the X line. *Geophysical Research Letters*, *43*, 6060–6069. <https://doi.org/10.1002/2016GL069212>
- Pollock, C., Moore, T., Jacques, A., Burch, J., Gliese, U., Saito, Y., et al. (2016). Fast plasma investigation for Magnetospheric Multiscale. *Space Science Reviews*, *199*(1–4), 331–406. <https://doi.org/10.1007/s11214-016-0245-4>
- Pritchard, K. R., Burch, J. L., Fuselier, S. A., Webster, J. M., Torbert, R. B., Argall, M. R., et al. (2019). Energy conversion and electron acceleration in the magnetopause reconnection diffusion region. *Geophysical Research Letters*, *46*, 10,274–10,282. <https://doi.org/10.1029/2019GL084636>
- Pritchett, P. L. (2001). Collisionless magnetic reconnection in a three-dimensional open system. *Journal of Geophysical Research*, *106*(A11), 25,961–25,977. <https://doi.org/10.1029/2001JA000016>
- Russell, C. T., Anderson, B. J., Baumjohann, W., Bromund, K. R., Dearborn, D., Fischer, D., et al. (2016). The Magnetospheric Multiscale magnetometers. *Space Science Reviews*, *199*(1–4), 189–256. <https://doi.org/10.1007/s11214-014-0057-3>
- Schwartz, S. J. (1998). Shock and discontinuity normals, Mach numbers, and related parameters. *ISSI Scientific Reports Series*, *1*, 249–270.
- Shay, M. A., Phan, T. D., Haggerty, C. C., Fujimoto, M., Drake, J. F., Malakit, K., et al. (2016). Kinetic signatures of the region surrounding the X line in asymmetric (magnetopause) reconnection. *Geophysical Research Letters*, *43*, 4145–4154. <https://doi.org/10.1002/2016GL069034>
- Shi, Q. Q., Shen, C., Pu, Z. Y., Dunlop, M. W., Zong, Q. G., Zhang, H., et al. (2005). Dimensional analysis of observed structures using multipoint magnetic field measurements: Application to Cluster. *Geophysical Research Letters*, *32*, L12105. <https://doi.org/10.1029/2005GL022454>
- Sonnerup, B., & Scheible, M. (1998). Analysis methods for multi-spacecraft data. *ISSI Scientific Report*.
- Torbert, R. B., Burch, J. L., Giles, B. L., Gershman, D., Pollock, C. J., Dorelli, J., et al. (2016). Estimates of terms in Ohm's law during an encounter with an electron diffusion region. *Geophysical Research Letters*, *43*, 5918–5925. <https://doi.org/10.1002/2016GL069553>
- Torbert, R. B., Burch, J. L., Phan, T. D., Hesse, M., Argall, M. R., Shuster, J., et al. (2018). Electron-scale dynamics of the diffusion region during symmetric magnetic reconnection in space. *Science*, *362*(6421), 1391–1395. <https://doi.org/10.1126/science.aat2998>
- Wang, R. S., Lu, Q., Nakamura, R., Baumjohann, W., Huang, C., Russell, C. T., et al. (2018). An electron-scale current sheet without bursty reconnection signatures observed in the near-Earth tail. *Geophysical Research Letters*, *45*, 4542–4549. <https://doi.org/10.1002/2017GL076330>
- Webster, J. M., Burch, J. L., Reiff, P. H., Daou, A. G., Genestreti, K. J., Graham, D. B., et al. (2018). Magnetospheric Multiscale dayside reconnection electron diffusion region events. *Journal of Geophysical Research: Space Physics*, *123*, 4858–4878. <https://doi.org/10.1029/2018JA025245>
- Xiao, C. J., Wang, X. G., Pu, Z. Y., Zhao, H., Wang, J. X., Ma, Z. W., et al. (2006). In situ evidence for the structure of the magnetic null in a 3D reconnection event in the Earth's magnetotail. *Nature Physics*, *2*(7), 478–483. <https://doi.org/10.1038/nphys342>

- Yamada, M., Kulsrud, R., & Ji, H. T. (2010). Magnetic reconnection. *Reviews of Modern Physics*, *82*(1), 603–664. <https://doi.org/10.1103/RevModPhys.82.603>
- Zhou, M., Deng, X. H., Zhong, Z. H., Pang, Y., Tang, R. X., el-Alaoui, M., et al. (2019). Observations of an electron diffusion region in symmetric reconnection with weak guide field. *The Astrophysical Journal*, *870*(1), 34. <https://doi.org/10.3847/1538-4357/aaf16f>